

PHYSICS

Tunable solidification of cornstarch under impact: How to make someone walking on cornstarch sink

Ran Niu^{1*†}, Meera Ramaswamy^{1†}, Christopher Ness^{2,3}, Abhishek Shetty⁴, Itai Cohen^{1*}

Hundreds of YouTube videos show people running on cornstarch suspensions demonstrating that dense shear thickening suspensions solidify under impact. Such processes are mimicked by impacting and pulling out a plate from the surface of a thickening cornstarch suspension. Here, using both experiments and simulations, we show that applying fast oscillatory shear transverse to the primary impact or extension directions tunes the degree of solidification. The forces acting on the impacting surface are modified by varying the dimensionless ratio of the orthogonal shear to the compression and extension flow rate. Simulations show varying this parameter changes the number of particle contacts governing solidification. To demonstrate this strategy in an untethered context, we show the sinking speed of a cylinder dropped onto the suspension varies markedly by changing this dimensionless ratio. These results suggest applying orthogonal shear while people are running on cornstarch would de-solidify the suspension and cause them to sink.

INTRODUCTION

The scientific demonstration of people running fast on the surface of a dense cornstarch suspension illustrates the propensity of mixtures consisting of solid particles in a fluid to solidify under impact. The formation of a solid plug under the impacting object leads to this marked increase in the normal force under fast compression or extension (1–4). Previous research has shown that this plug forms when particles in the suspension come into contact and form force chains (5–13). Thus, prior strategies to tune this solidification have focused on preventing the formation of these force chains in the first place by altering the volume fraction (14, 15), solvent composition (16, 17), or the physical properties of particles such as their size (8), shape (18–20), surface roughness (21–24), and polydispersity (25–27). These approaches, however, do not address whether it is possible to de-solidify a suspension once these force chains have already formed.

Here, we propose an active method to tune the solidification of dense shear thickening suspensions under rapid compression and extension by applying fast oscillatory shear transverse to the primary flow. Previous work showed that these orthogonal superimposed perturbations (OSP) can tune the viscosity of a thickened suspension under shear (28, 29). These papers suggest that by moving particles in a direction orthogonal to the maximum compressive axis, we can alter the particle trajectories and break up the contacts between particles. We hypothesize that this approach could be used to de-solidify the plug formed under a person's foot as they run on the surface of a cornstarch suspension.

RESULTS

We test this hypothesis in the context of extension and compression flows that imitate the process of a human foot lifting up and stepping

¹Department of Physics, Cornell University, Ithaca, NY 14853, USA. ²Department of Chemical Engineering and Biotechnology, University of Cambridge, Cambridge CB3 0AS, UK. ³School of Engineering, University of Edinburgh, Edinburgh EH9 3FB, UK. ⁴Anton Paar USA, 10215 Timber Ridge Drive, Ashland, VA 23005, USA.

*Corresponding author. Email: rn362@cornell.edu (R.N.); ic64@cornell.edu (I.C.)

†These authors contributed equally to this work.

down on the suspension surface. To perform our experiments, we modified a standard Anton Paar Twin Drive MCR 702 rheometer to incorporate a tunable oscillatory shear transverse to the primary compression or extension direction. To apply the orthogonal perturbations, we designed a custom-built attachment that oscillates the bottom plate about the vertical axis (see Materials and Methods and the Supplementary Materials for details). The top plate of the rheometer is used to retract from or compress a dense cornstarch suspension surface at constant strain rates along the vertical, z , direction. Schematics of the setup, coordinate definition, and flow geometry are shown in Fig. 1 (A and B). Using this apparatus, we determine the normal forces acting on the top impacting or retracting plate as a function of depth and the applied OSP.

We find that application of OSP markedly alters the suspension behavior under extension (Fig. 2, A and B). For a strain rate of $\dot{\gamma}_0 = 1.1 \text{ s}^{-1}$, comparable to that of a human walking on a 20-cm-deep cornstarch suspension, we observe brittle fracture as the plate is retracted from the surface (Fig. 2A and movie S1) (2, 30). The measured normal force F_N increases abruptly to a maximum value of $F_{\text{Max}} = 22 \text{ N}$ and rapidly vanishes as the suspension fractures (Fig. 2C). As we apply an OSP flow with a strain amplitude $\gamma_{\text{OSP}} = 24\%$ at progressively higher frequencies, we observe that the cornstarch plug de-solidifies, and the fracture transitions to a necking and pinch-off detachment characteristic of liquid droplet breakup (Fig. 2B and movie S2). The normal force on the retracting plate decreases by over an order of magnitude with increasing frequency (Fig. 2C). A similar decrease in normal force is observed with increasing OSP strain amplitude (see the Supplementary Materials). These results support our hypothesis that application of OSP flows can de-solidify plugs formed under extensional flows.

This decrease in the normal force suggests a relationship between the strain scale associated with force chain formation characterized by the extensional flow rate $\dot{\gamma}_0$ and the number and amplitude of the oscillations imposed by the orthogonal perturbations $2\pi f \gamma_{\text{OSP}}$. The strain applied by the OSP needs to be large enough to move the particles out of contact, and simultaneously, the frequency needs to be large enough to have at least one oscillation within the extensional strain required for the force chain turnover. Thus, we expect that

Copyright © 2020
The Authors, some
rights reserved;
exclusive licensee
American Association
for the Advancement
of Science. No claim to
original U.S. Government
Works. Distributed
under a Creative
Commons Attribution
NonCommercial
License 4.0 (CC BY-NC).

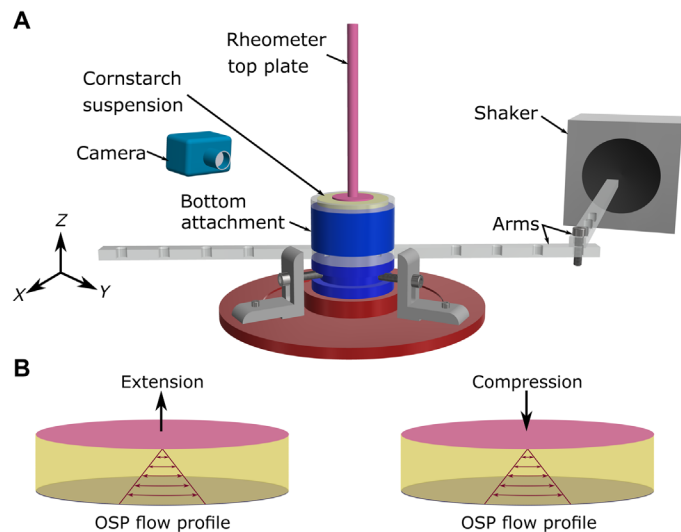


Fig. 1. Schematic of the experimental setup and flow geometries. (A) Schematic of the modified rheometer to apply tunable orthogonal perturbations. The top plate (pink) extrudes from or penetrates into the surface of the cornstarch suspension. The bottom attachment (blue) oscillates about a central pivot and is driven by a shaker that is connected via two arms that translate the horizontal motions of the shaker to the rotational oscillations of the sample. (B) Schematic illustrations of the experimental flow geometry and the orthogonal shear gradient in extension and compression experiments.

the number of force chains will decrease with the dimensionless ratio $\tilde{\Gamma} = 2\pi f \gamma_{\text{OSP}} / \dot{\gamma}_0$. We find that data for the maximum normal force normalized by the maximum normal force without OSP, $F_{\text{Max}}/F_{\text{Max}0}$, all scale with $\tilde{\Gamma}$ and collapse onto a single curve (Fig. 2D). These data, which span strain amplitudes from 5 to 89% and frequencies from 5 to 50 Hz, demonstrate that the transition of cornstarch suspensions from solid-like plugs to a liquid under application of OSP is governed by a single dimensionless parameter $\tilde{\Gamma}$.

We expect the normal force to depend on the number and orientation of particle contacts (6–12). Hence, we performed numerical simulations to gain insight into the microscopic details governing changes in normal force during extension with and without orthogonal perturbations. The simulation follows an established approach (5, 29, 31) that combines Stokes drag with short-range hydrodynamic and frictional contact interactions to model thickening suspensions (see Materials and Methods for more details). Here, the suspension is subjected to extensional flow with a superimposed orthogonal shear under conserved volume and periodic boundary conditions. We extract the time-averaged normal force, F_N , normalize it by the time-averaged normal force without OSP, F_{N0} , and report the normal force ratio F_N/F_{N0} versus $\tilde{\Gamma}$ in Fig. 2E (see the Supplementary Materials for time-dependent data). The simulation data show very similar trends to the experimental results. More specifically, we find that as $\tilde{\Gamma}$ increases beyond ~ 1 , the normal force ratio decreases by roughly an order of magnitude. As expected, the time-averaged particle contact number decreases with $\tilde{\Gamma}$ in a similar manner (Fig. 2F). We further characterize the time-averaged distribution of particle contact forces under extension projected onto the xz plane. Without OSP, the particle contacts mainly orient along the x direction corresponding to the maximum compressive axis. As OSP are applied and the average number of contacts decreases, the distribution of contact orientations becomes more homogeneous

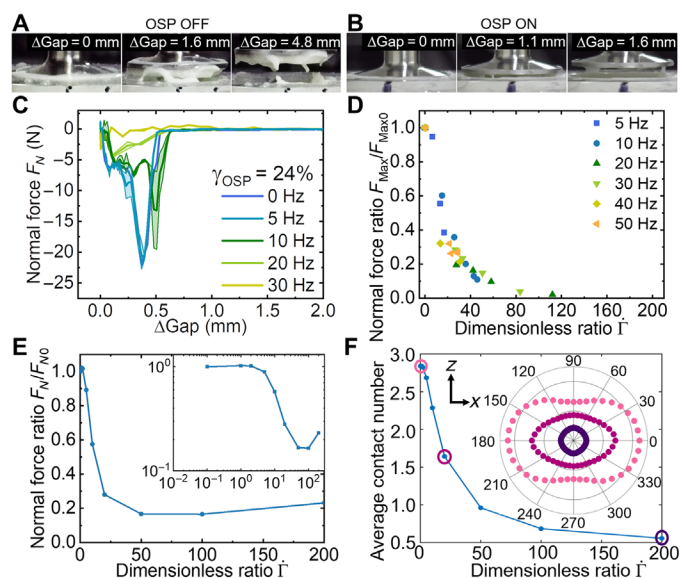


Fig. 2. The effect of OSP on uniaxial extension flows. (A) Snapshots of the extension experiment at different ΔGaps without OSP. (B) Snapshots of the extension experiment at different ΔGaps with orthogonal shear perturbations at a strain rate ratio of $\tilde{\Gamma} = 58.2$. (C) Normal force F_N versus ΔGap for different frequencies at a strain amplitude $\gamma_{\text{OSP}} = 24\%$. The shaded region bounding each curve indicates the measured variation in normal force. (D) Normal force ratio of the maximum normal force divided by the maximum normal force without orthogonal shear, $F_{\text{Max}}/F_{\text{Max}0}$, as a function of the dimensionless ratio $\tilde{\Gamma}$. Data are obtained from experiments where the OSP frequencies and amplitudes are varied. (E) Normal force ratio of the time-averaged normal force divided by the time-averaged normal force without orthogonal shear, F_N/F_{N0} , as a function of $\tilde{\Gamma}$. Data are obtained from simulations where the OSP frequency is varied. The inset shows a log-log plot of the same curve to illustrate the onset of de-solidification. (F) Average number of particle contacts versus $\tilde{\Gamma}$. The inset shows three representative radial distributions of particle-particle contacts projected onto the xz plane. The color of the three distributions plotted corresponds to the color and $\tilde{\Gamma}$ value of the three circled data points on the main plot. Photo credits: M. Ramaswamy (Cornell University).

(Fig. 2F, inset). Thus, despite the complicated nature of the flows characterizing solidifying suspension under extension, we find that application of OSP de-solidifies the plugs formed under the retracting plate.

Buoyed by these results, we test the effectiveness of our OSP protocol for de-solidifying plugs formed under rapid compression. We fix the compression strain rate at $\dot{\gamma} = 0.3 \text{ s}^{-1}$, which is a bit lower than that used for extension but allows for a larger range of measurements. In the absence of OSP, the normal force quickly increases to $\sim 50 \text{ N}$, the torque limit of the rheometer, within a penetration depth of a few hundred micrometers (Fig. 3A). As we apply OSP with a strain amplitude $\gamma_{\text{OSP}} = 5\%$ at progressively higher frequencies, this increase in the normal force is delayed to larger penetration depths (Fig. 3A). A similar increase in penetration depth is observed with increasing OSP strain amplitude (see the Supplementary Materials). We expect the same single parameter $\tilde{\Gamma}$ to regulate the de-solidification and de-thickening under compression. To verify this hypothesis, we plot the penetration depth where the normal force $F_N = 3 \text{ N}$ as a function of $\tilde{\Gamma}$. The penetration depths obtained at different frequencies (5 to 50 Hz) and amplitudes (2 to 10%) overlap, showing an increase of penetration depths with increasing $\tilde{\Gamma}$ (Fig. 3B). Thus, we find that similar to extensional flows,

the de-solidification and de-thickening under compression is indeed governed by the same dimensionless parameter $\dot{\Gamma}$.

To investigate the changes in the microstructure leading to de-solidification and de-thickening, we simulated rapid compression with superimposed orthogonal shear. We plot the time-averaged normal force normalized by the time-averaged normal force without OSP, F_N/F_{N0} , as a function of $\dot{\Gamma}$ in Fig. 3C. As $\dot{\Gamma}$ increases beyond ~ 1 , the normal force markedly decreases by roughly an order of magnitude. The time-averaged particle contact number also decreases with $\dot{\Gamma}$ in a similar manner (Fig. 3D). We further characterize the time-averaged distribution of particle contacts under compression projected onto the xz plane. In contrast to the extensional experiments, the particle contacts lie mainly along the z direction, the main compressive axis, for all values of $\dot{\Gamma}$. However,

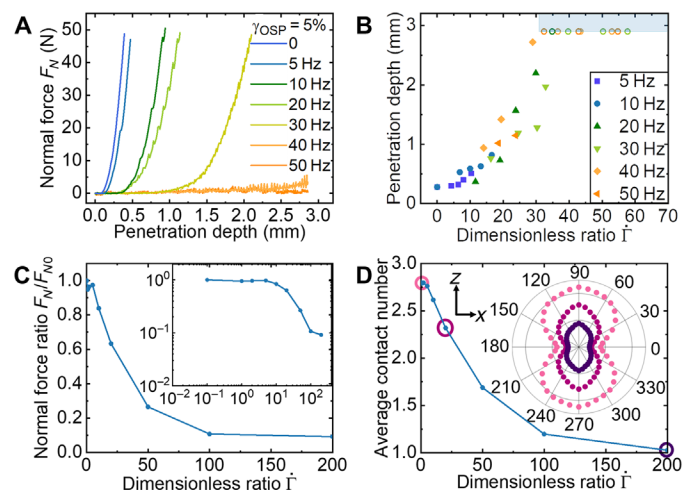


Fig. 3. The effects of OSP on rapid compression flows. (A) Normal force F_N as a function of penetration depth at different frequencies for $\gamma_{OSP} = 5\%$. (B) Penetration depth at which the measured normal force $F_N = 3\text{ N}$ versus the dimensionless ratio $\dot{\Gamma}$. Data where the penetration depth for $F_N = 3\text{ N}$ is greater than 2.9 mm—the upper bound of our measurement—are indicated by the shaded region. Data are obtained from experiments where the OSP frequencies and amplitudes are varied. (C) Normal force ratio of the time-averaged normal force divided by the time-averaged normal force without orthogonal shear, F_N/F_{N0} , versus dimensionless ratio $\dot{\Gamma}$. Data are obtained from simulations where the OSP frequency is varied. The inset shows a log-log plot of the same curve to illustrate the onset of de-solidification. (D) Average number of particle contacts versus $\dot{\Gamma}$. The inset shows three representative radial distributions of particle-particle contacts projected onto the xz plane. The color of the three distributions plotted corresponds to the color and $\dot{\Gamma}$ value of the three circled data points on the main plot.

as OSP are applied, the distribution of contact orientations becomes more homogeneous (Fig. 3D, inset). Thus, we find that while the details of the compression flows may be different from those under extension, a very similar de-solidification and de-thickening behavior is observed under application of OSP.

DISCUSSION

To demonstrate that these same de-thickening behaviors are relevant in an untethered context more similar to that of a human running on cornstarch, we test the effect of the orthogonal shear on the sinking speed of an object dropped onto the suspension surface. To quantify this effect, we use an electromagnet to release a cylinder from a given height and track the position of the cylinder as a function of time (Fig. 4A). The sedimentation speed is obtained from the initial slope of the curve. We find that orthogonal shear can drastically increase the sinking speed of the cylinder (Fig. 4B and movies S3 and S4). Similar to the case of the tethered rheometer setup, we expect the dimensionless ratio $\dot{\Gamma}$ to control the sedimentation speed. We find that when the sedimentation velocities are plotted as a function of $\dot{\Gamma}$, the data for different applied orthogonal frequencies and amplitudes overlap onto a single curve, thereby illustrating the applicability of this OSP method to untethered contexts (Fig. 4C).

These experiments also suggest that the OSP protocol can both de-solidify and de-thicken colloidal suspensions. For the extension experiments, the suspension demonstrates solid-like fracture, which subsequently becomes more liquid-like upon application of OSP. For the compression experiments, the prior literature suggests that a solid plug is formed under the impacting plate, but there is also strong shear thickening at the edges of the plug (1). Thus, the OSP protocol in the compression experiments may de-thicken the suspension, de-solidify the plug, or do both. Last, in the untethered case, the sinking of the cylinder into the suspension suggests that the suspension is shear thickened and not jammed. Thus, application of OSP de-thickens the suspension. The range of behavior observed here suggests that this OSP protocol and the governing dimensionless parameter are likely more general. Similar experiments on dense suspensions that transition between shear thickening and shear jammed states would elucidate the exact relationship between the applied OSP and the suspension flow behavior.

The ability of OSP to de-solidify plugs formed under extension and fast compression has potential industrial applications where it is important to increase the flow rate or control the viscosity or unclog a pipe. These applications range from high-throughput

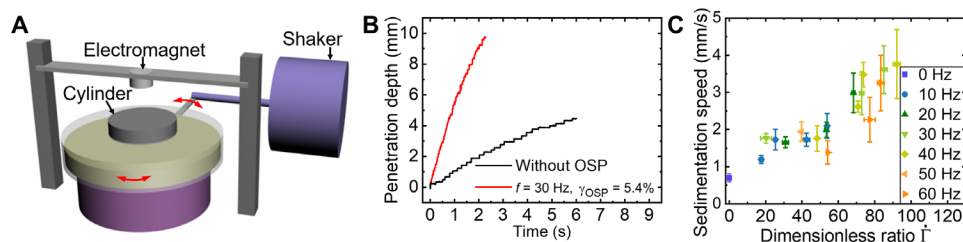


Fig. 4. Dependence of sinking speed on the applied OSP. (A) Schematic of the custom-built setup used to apply OSP and drop a cylinder onto the surface of a dense cornstarch suspension. A shaker and two lever arms were used to oscillate the suspension about a central axis. An electromagnet was used to release a stainless steel cylinder onto the suspension surface. (B) Penetration depth versus time for a cylinder 6 cm in diameter and 1.3 cm tall that is dropped onto the cornstarch suspension from a height of 4 cm. (C) Sedimentation speed of the cylinder after impact as a function of the dimensionless ratio $\dot{\Gamma}$. Error bars indicate standard deviations from five measurements.

processing of dense suspensions such as cement and concrete to avoid jamming in narrow pipes and three-dimensional printing. This technique could also have profound implications on the beloved science demonstration of a person running on cornstarch. For example, if OSP are applied as a person's foot is impacting the cornstarch surface, then the foot will rapidly sink into the cornstarch. In contrast, solidifying the suspensions by turning off the perturbations once the person's foot has sunk beneath the surface will make it extremely difficult to pull it out. Alternatively, applying perturbations as the person is pushing off the cornstarch surface will substantially reduce the normal forces and make it more difficult, if not impossible, to run on the suspension. These are just some of the ideas that we hope will inspire the next generation of video demonstrations aimed at highlighting the astonishing properties of this ubiquitous yet unexpectedly curious and fascinating material.

MATERIALS AND METHODS

Sample preparation

Suspensions of solid fraction 54 weight % (wt %) (upper limit of workable solid content) were prepared by dispersing weighted amounts of dry cornflour (Argo) in a 50 wt% water/glycerol (Sigma-Aldrich) mixture, followed by intensive hand mixing for ~20 min. After mixing, the freshly prepared suspensions were left undisturbed for 30 min before use. Because of the high porosity of the particles (around 30%), cornstarch adsorbs solvent and continuously expands in suspension. Therefore, to achieve repeatable measurements, all the experiments were conducted within 30 min. Since our experiments last only a few seconds, we did not observe any substantial time-dependent behavior associated with processes such as sedimentation.

Experimental setup

We attached a custom-built bottom plate onto a standard Anton Paar Twin Drive MCR 702 rheometer to couple a tunable orthogonal oscillatory shear with the primary extensional flows. We translated the rheometer top plate (cone-plate geometry with a diameter of 25 mm and a cone of 1°) in the z direction at constant strain rates to generate extensional and compressive flows. The bottom plate was used to apply the tunable orthogonal shear. Oscillations were achieved by coupling the bottom plate to a vibrating shaker (Type4808, Brüel & Kjær North America Inc.) via two arms. The arms rotated the bottom plate about a central pivot to generate rotational motions. Special care was taken to ensure the sample cell is flat, and the OSP is only applied in the orthogonal direction (see the Supplementary Materials for details and OSP calibration). A fast camera (GoPro) was used to record the oscillations of the sample cell at a frame rate of 120 Hz, from which we tracked the frequency and amplitude of the orthogonal shear.

To conduct the uniaxial extension experiments, a custom-made sample cell with an outer diameter of 50.8 mm, an inner diameter of 35 mm, and a depth of 1.9 mm was fixed to the bottom plate. Before the start of the extension, the plate was immersed 1 mm into the suspension corresponding to about the plate thickness. To conduct the compression experiments, samples of a depth of 5 mm were prepared in a glass petri dish with an outer diameter of 50 mm, an inner diameter of 48 mm, and a depth of 7 mm. Before the start of the compression experiments, the top plate of the rheometer was immersed 1 mm into the cornstarch suspension. The shear and oscillatory

rheology measured by conventional techniques are given in the Supplementary Materials.

Numerical simulation

We used numerical simulations to observe the distribution and number of particle contacts under shear. A uniaxial extension or compression is applied along the z axis, and the fast orthogonal perturbations are applied with the gradient along the xz plane. This geometry mimics a fluid element in the experiments. We model the trajectories of suspended particles under combined compression/extension and orthogonal oscillatory flow. The simulation follows an established approach (5, 29, 31), combining Stokes drag with short-range hydrodynamic and frictional contact interactions and operating in the non-Brownian, noninertial regime corresponding to a shear-thickened state. The periodic simulation box contains 15,000 particles (1:1 mixture of size ratio 1:1.4) at volume fraction $\phi = 0.56$ and is subjected to volume conserving deformations corresponding to biaxial and uniaxial extensions with superimposed oscillations. The ratio of the oscillatory rate to extensional rate $\bar{\Gamma}$ (defined in the Supplementary Materials) is the only relevant control parameter for the simulation. From the evolving particle positions, we can interrogate the arrangement of particle-particle contacts and calculate the stress tensor, from which normal forces and viscosity are obtained as a function of $\bar{\Gamma}$. Further model details are given in the Supplementary Materials.

SUPPLEMENTARY MATERIALS

Supplementary material for this article is available at <http://advances.sciencemag.org/cgi/content/full/6/19/eaay6661/DC1>

REFERENCES AND NOTES

1. E. Han, I. R. Peters, H. M. Jaeger, High-speed ultrasound imaging in dense suspensions reveals impact-activated solidification due to dynamic shear jamming. *Nat. Comm.* **7**, 12243 (2016).
2. S. Majumdar, I. R. Peters, E. Han, H. M. Jaeger, Dynamic shear jamming in dense granular suspensions under extension. *Phys. Rev. E* **95**, 012603 (2017).
3. E. E. B. White, M. Chellamuthu, J. P. Rothstein, Extensional rheology of a shear-thickening cornstarch and water suspension. *Rheol. Acta* **49**, 119–129 (2010).
4. S. R. Waitukaitis, H. M. Jaeger, Impact-activated solidification of dense suspensions via dynamic jamming fronts. *Nature* **487**, 205–209 (2012).
5. O. Cheal, C. Ness, Rheology of dense granular suspensions under extensional flow. *J. Rheol.* **62**, 501–512 (2018).
6. J. Comtet, G. Chatté, A. Niguès, L. Bocquet, A. Siria, A. Colin, Pairwise frictional profile between particles determines discontinuous shear thickening transition in non-colloidal suspensions. *Nat. Comm.* **8**, 15633 (2017).
7. R. Seto, R. Mari, J. F. Morris, M. M. Denn, Discontinuous shear thickening of frictional hard-sphere suspensions. *Phys. Rev. Lett.* **111**, 218301 (2013).
8. B. M. Guy, M. Hermes, W. C. K. Poon, Towards a unified description of the rheology of hard-particle suspensions. *Phys. Rev. Lett.* **115**, 088304 (2015).
9. T. S. Majumdar, R. P. Behringer, Contact force measurements and stress-induced anisotropy in granular materials. *Nature* **435**, 1079–1082 (2005).
10. J. R. Royer, D. L. Blair, S. D. Hudson, Rheological signature of frictional interactions in shear thickening suspensions. *Phys. Rev. Lett.* **116**, 188301 (2016).
11. D. Bi, J. Zhang, B. Chakraborty, R. P. Behringer, Jamming by shear. *Nature* **480**, 355–358 (2011).
12. A. Zaccone, D. Gentili, H. Wu, M. Morbidelli, E. Del Gado, Shear-driven solidification of dilute colloidal suspensions. *Phys. Rev. Lett.* **106**, 138301 (2011).
13. R. Radhakrishnan, J. R. Royer, W. C. K. Poon, J. Sun, Force chains and networks: wet suspensions through dry granular eyes. *Granul. Matter* **22**, 29 (2020).
14. J. C. van der Werff, C. G. de Kruijff, Hard-sphere colloidal dispersions: The scaling of rheological properties with particle size, volume fraction, and shear rate. *J. Rheol.* **33**, 421–454 (1989).
15. N. J. Wagner, J. F. Brady, Shear thickening in colloidal dispersions. *Phys. Today* **62**, 27–32 (2009).
16. N. M. James, E. Han, R. A. L. de la Cruz, J. Jureller, H. M. Jaeger, Interparticle hydrogen bonding can elicit shear jamming in dense suspensions. *Nat. Mater.* **17**, 965–970 (2018).

17. N. Park, V. Rathee, D. L. Blair, J. C. Conrad, Contact networks enhance shear thickening in attractive colloid-polymer mixtures. *Phys. Rev. Lett.* **122**, 228003 (2019).
18. S. Majumdar, R. Krishnaswamy, A. K. Sood, Discontinuous shear thickening in confined dilute carbon nanotube suspensions. *Proc. Natl. Acad. Sci. U.S.A.* **108**, 8996–9001 (2011).
19. N. M. James, H. Xue, M. Goyal, H. M. Jaeger, Controlling shear jamming in dense suspensions via the particle aspect ratio. *Soft matter* **15**, 3649–3654 (2019).
20. F. Tapia, S. Shaikh, J. E. Butler, O. Pouliquen, E. Guazzelli, Rheology of concentrated suspensions of non-colloidal rigid fibres. *J. Fluid Mech.* **827**, 10.1017/jfm.2017.552, (2017).
21. L. C. Hsiao, S. Jamali, E. Glynos, P. F. Green, R. G. Larson, M. J. Solomon, Rheological state diagrams for rough colloids in shear flow. *Phys. Rev. Lett.* **119**, 158001 (2017).
22. D. Lootens, H. van Damme, Y. Hémar, P. Hébraud, Dilatant flow of concentrated suspensions of rough particles. *Phys. Rev. Lett.* **95**, 268302 (2005).
23. C.-P. Hsu, S. N. Ramakrishna, M. Zanini, N. D. Spencer, L. Isa, Roughness-dependent tribology effects on discontinuous shear thickening. *Proc. Natl. Acad. Sci. U.S.A.* **115**, 5117–5122 (2018).
24. V. Rathee, S. Arora, D. L. Blair, J. S. Urbach, A. K. Sood, R. Ganapathy, Unraveling the role of frictional contacts and particle orientational order during shear-thickening in suspensions of colloidal rods. arXiv:1906.06356 (2019).
25. Y. Madraki, S. Hormozi, G. Ovarlez, E. Guazzelli, O. Pouliquen, Enhancing shear thickening. *Phys. Rev. Fluids* **2**, 033301 (2017).
26. B. J. Maranzano, N. J. Wagner, The effects of particle size on reversible shear thickening of concentrated colloidal dispersions. *J. Chem. Phys.* **114**, 10514–10527 (2001).
27. Y. Madraki, G. Ovarlez, S. Hormozi, Transition from continuous to discontinuous shear thickening: An excluded-volume effect. *Phys. Rev. Lett.* **121**, 108001 (2018).
28. N. Y. C. Lin, C. Ness, M. E. Cates, J. Sun, I. Cohen, Tunable shear thickening in suspensions. *Proc. Natl. Acad. Sci. U.S.A.* **113**, 10774–10778 (2016).
29. C. Ness, R. Mari, M. E. Cates, Shaken and stirred: Random organization reduces viscosity and dissipation in granular suspensions. *Sci. Adv.* **4**, eaar3296 (2018).
30. M. I. Smith, R. Besseling, M. E. Cates, V. Bertola, Dilatancy in the flow and fracture of stretched colloidal suspensions. *Nat. Comm.* **1**, 114 (2010).
31. C. Ness, J. Sun, Flow regime transitions in dense non-brownian suspensions: Rheology, microstructural characterization, and constitutive modeling. *Phys. Rev. E* **91**, 012201 (2015).
32. F. Boyer, É. Guazzelli, O. Pouliquen, Unifying suspension and granular rheology. *Phys. Rev. Lett.* **107**, 188301 (2011).
33. R. Radhakrishnan, Derivation of lubrication forces for unequal spheres. 10.5281/zenodo.1137305 (2017).
34. S. Kim, S. Karrila, *Microhydrodynamics: Principles and Selected Applications* (Butterworth-Heinemann, Boston, 1991).
35. S. Plimpton, Fast parallel algorithms for short-range molecular dynamics. *J. Comput. Phys.* **117**, 1–19 (1995).

Acknowledgments: We thank Anton Paar for use of the Twin Drive MCR 702 rheometer through the VIP academic research program and the Cohen group for insightful suggestions.

Funding: This work is supported by NSF CBET award numbers 1804963 and 1509308 as well as DMR-1507607 and the Cornell MRSEC DMR-1719875. C.N. acknowledges financial support from the Maudslay-Butler Research Fellowship at Pembroke College, Cambridge and latterly from the Royal Academy of Engineering under the Research Fellowship scheme.

Author contributions: I.C., R.N., and M.R. conceived the experiments and experimental design. M.R. constructed the apparatus. A.S. helped set up the modifications to the rheometer and determine the experimental protocol. R.N. ran most of the experiments and analyzed the experimental data. C.N. conducted the simulations. C.N. and M.R. analyzed the simulation data. R.N., M.R., and I.C. wrote the manuscript with all authors contributing. **Competing interests:** The authors declare that they have no competing interests. **Data and materials availability:** All data needed to evaluate the conclusions in the paper are present in paper and/or the Supplementary Materials. Additional data related to this paper may be requested from the authors.

Submitted 9 July 2019

Accepted 27 February 2020

Published 8 May 2020

10.1126/sciadv.aay6661

Citation: R. Niu, M. Ramaswamy, C. Ness, A. Shetty, I. Cohen, Tunable solidification of cornstarch under impact: How to make someone walking on cornstarch sink. *Sci. Adv.* **6**, eaay6661 (2020).

Tunable solidification of cornstarch under impact: How to make someone walking on cornstarch sink

Ran Niu, Meera Ramaswamy, Christopher Ness, Abhishek Shetty and Itai Cohen

Sci Adv 6 (19), eaay6661.
DOI: 10.1126/sciadv.aay6661

ARTICLE TOOLS

<http://advances.sciencemag.org/content/6/19/eaay6661>

SUPPLEMENTARY MATERIALS

<http://advances.sciencemag.org/content/suppl/2020/05/04/6.19.eaay6661>

REFERENCES

This article cites 31 articles, 4 of which you can access for free
<http://advances.sciencemag.org/content/6/19/eaay6661#BIBL>

PERMISSIONS

<http://www.sciencemag.org/help/reprints-and-permissions>

Use of this article is subject to the [Terms of Service](#)

Science Advances (ISSN 2375-2548) is published by the American Association for the Advancement of Science, 1200 New York Avenue NW, Washington, DC 20005. The title *Science Advances* is a registered trademark of AAAS.

Copyright © 2020 The Authors, some rights reserved; exclusive licensee American Association for the Advancement of Science. No claim to original U.S. Government Works. Distributed under a Creative Commons Attribution NonCommercial License 4.0 (CC BY-NC).